Delft University of Technology

Experimental study of air–water flow properties in the breaking roller of dam-break waves

Regout, D.; Jonkman, S. N.; Wüthrich, D.

DOI
10.1016/j.ijmultiphaseflow.2024.105119

Publication date
2025

Document Version
Final published version

Published in
International Journal of Multiphase Flow

Citation (APA)
Regout, D., Jonkman, S. N., & Wüthrich, D. (2025). Experimental study of air–water flow properties in the breaking roller of dam-break waves. *International Journal of Multiphase Flow*, *185*, Article 105119. https://doi.org/10.1016/j.ijmultiphaseflow.2024.105119

Important note
To cite this publication, please use the final published version (if applicable).
Please check the document version above.

Copyright
Other than for strictly personal use, it is not permitted to download, forward or distribute the text or part of it, without the consent of the author(s) and/or copyright holder(s), unless the work is under an open content license such as Creative Commons.

Takedown policy
Please contact us and provide details if you believe this document breaches copyrights.
We will remove access to the work immediately and investigate your claim.

This work is downloaded from Delft University of Technology.
For technical reasons the number of authors shown on this cover page is limited to a maximum of 10.

International Journal of Multiphase Flow 185 (2025) 105119

Contents lists available at ScienceDirect

International Journal of Multiphase Flow

journal homepage: www.elsevier.com/locate/ijmulflow

Research Paper

Experimental study of air–water flow properties in the breaking roller of dam-break waves

D. Regout *, S.N. Jonkman, D. Wüthrich

Department of Hydraulic Engineering, Delft University of Technology, Stevinweg 1, Delft, 2628 CN, The Netherlands

ARTICLE INFO

Keywords:
Air–water flow properties
Dam-break waves
Highly unsteady flows
Long-period waves
Physical modeling
Breaking roller

ABSTRACT

Dam-break waves are highly unsteady long-wave phenomena, characterized by a breaking front with a strong recirculating air–water mixture. While the air–water flow properties of steady flows have often been investigated, the understanding of dynamic processes in unsteady multiphase flows remains limited. In this experimental study, a new approach was implemented to analyze the air–water flow properties of highly unsteady flows in the form of dam-break waves using ensemble-averaging techniques to account for short-duration measurements. The new dataset includes four different flow conditions, providing novel insights into the relation between various hydrodynamic characteristics and key air–water flow properties, including bubble characteristics and void fraction. The void fraction profiles indicated the presence of a turbulent shear layer along with a recirculation zone close to the free surface, showing analogies with similar steady and unsteady flow phenomena. Variations in the Froude number were shown to strongly affect the number and size of air bubbles, particularly in the shear layer. Higher depth-averaged air concentrations were found with increasing Froude numbers, reaching up to 40% for Fr = 5.14. Overall, the results confirm the importance of considering the presence of air in dam-break waves and demonstrate the suitability of this new methodology for investigating air–water flow properties in highly turbulent flows. They offer a deeper understanding of the multiphase nature of dam-break waves, which is relevant for a wide range of processes in coastal and hydraulic engineering.

1. Introduction

Dam-break waves propagating over wet bed are unsteady, high-translatory wave phenomena with a breaking front, characterized by a strong recirculating air–water mixture. Their flow properties have been studied for decades and often used as analogies to reproduce the behavior of various long-period wave events such as tsunamis, impulse waves, storm surges, and flash floods (Chanson, 2004a; Madsen et al., 2008; Wüthrich et al., 2018). Interactions of these phenomena with built environments can lead to severe impacts, including infrastructural damage and potential loss of life. The presence of air in the highly aerated wavefront, which remains poorly understood, significantly influences processes that modify hydrodynamic behavior (Lubin and Chanson, 2017). Moreover, numerous studies have emphasized the critical role of aeration in wave–structure interactions, with compressibility becoming a key factor; affecting peak pressure magnitudes, impact duration, and inducing oscillations in the structural response (Bullock et al., 2007; Nouri et al., 2010; Zuo et al., 2022). These factors underscore the importance of quantifying air within the approaching wavefronts to improve the understanding of their complex and turbulent hydrodynamic behavior. Such insights are essential for a wide range of applications, including assessing wave-impact loads on coastal and hydraulic structures, green-water loads on ships, and validating numerical models (Al-Faesly et al., 2012; Ryu et al., 2007; Yang et al., 2022).

Dam-break waves are defined as a single wave caused by the sudden release of a large body of water due to the failure of a water-retaining structure. This generates a gravity-driven positive surge propagating downstream, resulting in abrupt discontinuities in water levels, velocities, and pressures. The first analytical approach to describe the non-linear free-surface deformation and wavefront celerity was provided by Ritter (1892), using a simplified model based on the one-dimensional Shallow Water Equations (SWE) for a rectangular, horizontal smooth channel, assuming an infinite reservoir and an ideal fluid. Many studies elaborated on Ritter's formulation, highlighting the significant effects of bed roughness, frictional resistance, and turbulence at the wavefront (Dressler, 1952; Whitham, 1955; Chanson, 2009). Stoker (1957) expanded on Ritter's work by analyzing a dam-break wave over still water. He provided an analytical expression

* Corresponding author.
E-mail address: d.regout@tudelft.nl (D. Regout).

https://doi.org/10.1016/j.ijmultiphaseflow.2024.105119
Received 16 July 2024; Received in revised form 25 November 2024; Accepted 27 December 2024
Available online 6 January 2025
0301-9322/© 2025 The Authors. Published by Elsevier Ltd. This is an open access article under the CC BY-NC-ND license (http://creativecommons.org/licenses/by-nc-nd/4.0/).

for the breaking bore that develops over a certain distance, which is characterized by a strong recirculating air–water mixture with significant air entrainment, induced by shear effects due to the water level downstream (Wüthrich et al., 2021). Numerous studies investigated dam-break waves over wet beds, examining the relation between tailwater depths and free-surface dynamics, including the free-surface profile, wave celerity, and bed roughness effects, both experimentally (Stansby et al., 1998; Çağatay and Kocaman, 2008; Zhou et al., 2024; Yang et al., 2022; Nielsen et al., 2022) and numerically (Ozmen-Cagatay and Kocaman, 2010; Yang et al., 2018; Ye et al., 2020). While these emphasized the dominant non-linear effects influencing the breaking roller characteristics, most studies focused on predicting (local) velocities and free-surface dynamics, paying little attention to quantifying the air–water flow properties within the broken wavefront.

The presence of air significantly influences dynamic processes, leading to substantial changes in flow properties. Air–water interactions, also known as multiphase or two-phase flows, involve viscous, surface tension, and gravitational effects, which result in turbulent free-surface features, eddy formation, and bubble structures (Brocchini and Peregrine, 2001; Wüthrich et al., 2021). The use of phase-detection probes and high-speed video cameras advanced the understanding of these complex flows. However, most experimental studies focused on steady flow phenomena, particularly hydraulic jumps, as summarized in Table 1. Among them, Wang and Murzyn (2017) examined characteristic turbulent scales in hydraulic jumps across the entire water column, while Montano and Felder (2020) and Chachereau and Chanson (2011a) analyzed air–water flow properties, focusing on bubble characteristics, void fraction, and interfacial velocities. Most recently, Wüthrich et al. (2022b) studied air–water surface patterns and the transverse distribution of two-phase flow properties in hydraulic jumps with low Froude numbers, pointing out similarities with unsteady flows. Multiple of these studies have identified distinct regions across the roller of a hydraulic jump, each influenced by different physical processes and linked to variations in air distribution. However, the steady nature allows for long-duration measurements of the highly turbulent behavior, an approach not feasible for unsteady dam-break waves. Research on the multiphase behavior of unsteady flows is limited, mostly based on small datasets. Chanson (2004b) studied the air–water flow properties of unsteady open-channel flows over a sloped bed with a stepped invert. Leng and Chanson (2019) and Wüthrich et al. (2022a) measured air–water flow properties in breaking bores using phase-detection probes and introduced a novel ensemble-averaging approach based on multiple repetitions to compensate for short-duration measurements. Shi et al. (2023a,b) visualized air–water interactions and velocity profiles in breaking bores using image-processing techniques, comparing them to probe data. These studies addressed the influence of air distribution on physical processes, with results showing similarities with steady flow phenomena. Nevertheless, they were mostly limited to bores propagating on an initial flow with non-zero velocities and two comparatively low Froude numbers. While dam-break waves have been commonly studied and their multiphase nature is frequently mentioned to influence their behavior, no studies so far have quantified or analyzed the air–water flow properties in these waves. Hence, the lack of availability and diversity of experimental data restrict the understanding of how these unsteady multiphase flows behave under different hydrodynamic conditions.

In parallel, new developments in Computational Fluid Dynamics (CFD) enhanced the quantity and quality of numerical simulations investigating multiphase flows. While most advanced CFD methods are increasingly capable of reproducing turbulent processes, few multiphase flow models incorporate air (Ma et al., 2011; Witt et al., 2015; Mortazavi et al., 2016; Zabaleta et al., 2023). The current lack of quantitative empirical knowledge of air–water flow properties in highly unsteady flows also hinders the development of numerical models, which require high-quality experimental data to validate and compare their performance.

Therefore, this experimental study was conducted to address the clear need for quantitative knowledge on the multiphase nature of the breaking roller in highly unsteady flows, represented by dam-break waves over wet beds. A new approach for measuring air in unsteady flows was implemented using ensemble-averaging techniques to account for short-duration measurements. This allowed for a detailed and comprehensive investigation and comparison of air–water interactions across different flow conditions. Consequently, this research provides novel insights into key air–water flow properties that significantly influence the turbulent hydrodynamic behavior of the broken wavefront. The experimental setup and signal processing are detailed in Sections 2 and 3, respectively. Section 5 presents results on the free surface characteristics, followed by Section 6 which discusses air–water flow properties, covering bubble characteristics (size and quantity) and void fraction. Finally, void fraction profiles are compared to various analytical models in Section 7, with a conclusion presented in Section 8.

2. Experimental set-up and flow conditions

The experimental setup and flow conditions are based on the theoretical framework described by Stoker (1957), briefly introduced below.

2.1. 1D dam-break wave characteristics

Stoker's theory describes the 1D nonlinear dam-break wave profile propagating over a still water level by combining Ritter's solution for dry-bed conditions with a shock wave at the wavefront, which depends on the upstream (d_0) and downstream (h_0) flow depth ratio (Stoker, 1957). It describes a typical longitudinal free-surface profile, featuring a rounded wavefront that propagates with a constant celerity U, followed by a constant water level known as the plateau height h_p (see Fig. 1a). The plateau height h_p and wavefront celerity U are therefore commonly used as indicative characteristics in numerous dam-break wave studies (Chanson, 2004a; Arnason, 2005; Yang et al., 2018).

2.2. Experimental set-up and flow conditions

New experiments were conducted at the Hydraulic Engineering Laboratory of Delft University of Technology, the Netherlands, where dam-break waves were generated in a large horizontal flume 39 m long, 0.76 m wide, and 0.85 m deep, with a smooth concrete bed. A newly designed pneumatic lift gate system enforced an abrupt opening, releasing ca. 12.2 m^3 of water, to generate a dam-break wave with a broken wavefront propagating with a celerity U over a still tailwater depth h_0 (Fig. 1a). The gate opening time t adhered to the criterion of Lauber and Hager (1998), $t < \sqrt{2d_0/g}$, preventing any interference of the gate opening with the wave properties. Throughout all experiments, impoundment depth $d_0 = 0.8$ m remained constant, while different flow conditions were achieved by varying the downstream tailwater depth h_0, as summarized in Table 2. The dam-break waves are characterized by the Froude number $\mathrm{Fr} = U/(\sqrt{gh_0})$ and Reynolds number $\mathrm{Re} = (\rho U h_0)/\mu$, with water density $\rho = 1000$ kg m^{-3}, and dynamic viscosity $\mu = 1.002 \cdot 10^{-3}$ Pa·s.

Four Acoustic Displacement Meters (ADMs), microsonic-type mic+35/IU/TC, were positioned along the centerline of the flume downstream of the gate at positions $x/d_0 = 11.68$, 12.93, 14.18, 16.68 (Fig. 1a). The acoustic sensors collected echo propagation time measurements to record changes in water level, with a response time less than 64 ms and a precision of ± 0.1 mm. The ADM data is used to analyze free-surface profiles, including the plateau height h_p, and to calculate wavefront celerity as the ratio of the distance between sensors over the traveling time ($U = \Delta x/\Delta t$). In addition, the waves were recorded using DSLR and high-speed video cameras.

Air–water flow properties were measured using an array of four double-tip phase-detection conductivity probes manufactured by the

Table 1
Selected previous experimental research on air–water flow properties using conductivity probes.

	Reference	Fr	Re	d [m]	V_1 [m/s]
Hydraulic jump	Murzyn et al. (2005)	2.0 to 4.8	$8.8 \cdot 10^4$ to $4.58 \cdot 10^4$	0.059 to 0.021	1.50 to 2.19
	Chanson (2007)	4.6 to 8.6	$0.2 \cdot 10^5$ to $1.15 \cdot 10^5$	0.012 to 0.029	1.7 to 4.0
	Chachereau and Chanson (2011b)	3.1 to 5.1	$0.89 \cdot 10^5$ to $1.3 \cdot 10^5$	0.044 to 0.0395	2.6 to 3.57
	Wang (2014)	3.8 to 10.0	$3.4 \cdot 10^4$ to $9.5 \cdot 10^4$	0.0206 to 0.021	1.74 to 4.53
	Wang and Murzyn (2017)	7.5	$0.34 \cdot 10^5$ to $1.4 \cdot 10^5$	0.0129 to 0.033	2.67 to 4.27
	Kramer and Valero (2020)	4.25	$1.15 \cdot 10^5$	0.042	2.73
	Montano and Felder (2020)	1.8 to 4.6	$4.0 \cdot 10^5$ to $0.5 \cdot 10^5$	0.170 to 0.023	4.71 to 3.62
	Bai et al. (2021)	5.1	$9.0 \cdot 10^5$	1.1	6.1
	Estrella et al. (2022a,b)	1.9, 2.1	$7.75 \cdot 10^3$, $0.29 \cdot 10^5$ to $3.05 \cdot 10^5$	0.012, 0.027 to 0.130	0.65, 1.08 to 2.36
	Wüthrich et al. (2022b)	2.1, 2.4	$2.03 \cdot 10^5$, $1.86 \cdot 10^5$	0.097, 0.084	2.1, 2.21
Breaking bore	Leng and Chanson (2019)	2.1*	$2.06 \cdot 10^5$**	0.097	1.49***
	Wüthrich et al. (2022a)	2.1*, 2.4*	$2.03 \cdot 10^5$**, $1.86 \cdot 10^5$**	0.097, 0.084	1.47*** , 1.71****
	Shi et al. (2023a,b)	2.4*	$2.3 \cdot 10^5$**	0.084	1.71****

* Froude number of breaking bore is defined as $\mathrm{Fr} = (V_1 + U) \cdot (g \cdot d)^{-0.5}$.
** Reynolds number of breaking bore is defined as $\mathrm{Re} = \rho \cdot (V_1 + U) \cdot d \cdot \mu^{-1}$.
*** In addition to the inflow velocity V_1, the breaking bore had an upstream bore velocity of $U = 0.64$ m/s in the opposite direction.
**** In addition to the inflow velocity V_1, the breaking bore had an upstream bore velocity of $U = 0.51$ m/s in the opposite direction.

Table 2
Test program and the characteristics of the tested flow conditions.

Flow condition	d_0 [m]	h_0 [m]	$\frac{h_0}{d_0}$	h_p [m]	U [m/s]	Fr	Re	Repetitions
FC1	0.8	0.032	0.04	0.223	2.88	5.14	$0.92 \cdot 10^5$	220
FC2	0.8	0.064	0.08	0.290	2.82	3.56	$1.80 \cdot 10^5$	220
FC3	0.8	0.096	0.12	0.333	2.75	2.83	$2.63 \cdot 10^5$	220
FC4	0.8	0.128	0.16	0.367	2.73	2.44	$3.49 \cdot 10^5$	220

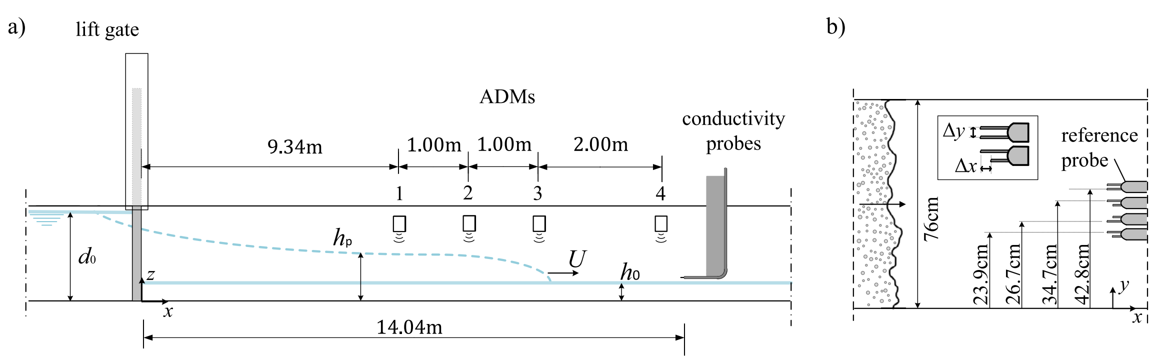

Fig. 1. (a) Side-view sketch of the experimental set-up with $d_0 = 0.8$ m, (b) Top-view sketch with details of the phase-detection probe array.

University of Queensland, Australia. Changes in conductivity are detected when the tips are exposed to air bubbles (low conductivity) or water (high conductivity). Each probe tip consists of a silver inner electrode ($\varnothing = 0.25$ mm) and a stainless-steel outer electrode ($\varnothing = 0.8$ mm), spaced transversely by $\Delta y = 1.8$ mm. Shown in Fig. 1b, the reference probe is equipped with two leading tips ($\Delta x = 0$ mm), while the other probes have a leading and trailing tip with a longitudinal spacing of $\Delta x = 6.3$ mm. Positioned downstream of the gate at $x/d_0 = 17.55$, all four probes are aligned at different elevations and sampled simultaneously at 100 kHz. Four probe configurations were tested for each flow condition, with three probes shifted vertically to cover 13 elevations (h_0 - 10 mm $< z < h_0$ + 210 mm), while the reference probe remained fixed 5 mm above the initial water level to ensure synchronization across repetitions. Due to the unsteadiness of the flow, long-duration measurements were not possible. Therefore, data analysis applied ensemble-averaging approach, which required a significant number of repetitions (Wüthrich et al., 2022a). Consequently, each configuration was tested 55 times per elevation, resulting in $n = 220$ repetitions for each flow condition.

Froude scaling laws are essential for accurately simulating gravitational and inertial forces in free surface flows at the laboratory scale (Pfister and Chanson, 2014). However, relying solely on Froude similarity may not fully capture scale effects in multiphase flows, particularly those involving surface tension and viscous forces, associated with the Weber and Reynolds number, respectively. The Reynolds number is defined as $\mathrm{Re} = (\rho U h_0)/\mu$, and the Weber number as $\mathrm{We} = (\rho h_0 U^2)/\sigma$, where h_0 is the initial still water level, U is the wavefront celerity, ρ is the water density, μ is the dynamic viscosity, and σ is the surface tension. In addition, the Morton number is used: $\mathrm{Mo} = \mathrm{We}^3/(\mathrm{Fr}^2\mathrm{Re}^4)$, achieving Morton similitude when the fluid is the same in both model and prototype (Chesters, 1975; Pfister and Hager, 2014). This study considered Froude and Morton similitude with the Reynolds number $0.92 \cdot 10^5 < \mathrm{Re} < 3.49 \cdot 10^5$ and Weber number $62 < \mathrm{We}^{0.5} < 117$, sufficiently high to minimize scale effects, as recommended by Fuchs (2013), Pfister and Chanson (2014), and Estrella et al. (2022b).

3. Signal processing and characteristic parameters

Phase-detection probes detect the presence of air through changes in conductivity, capturing a voltage drop when the probe tip is exposed to air. Since phase changes are often non-instantaneous and affected by wetting/drying processes, a single-threshold technique is commonly applied to distinguish air and water (Cartellier and Achard, 1991). The raw voltage signal V is then converted into a binary signal of the instantaneous void fraction c, defined as:

$$c(t) = \begin{cases} 0\,(\text{water}) & \text{if} \quad V > V_T \\ 1\,(\text{air}) & \text{if} \quad V < V_T\,. \end{cases}$$

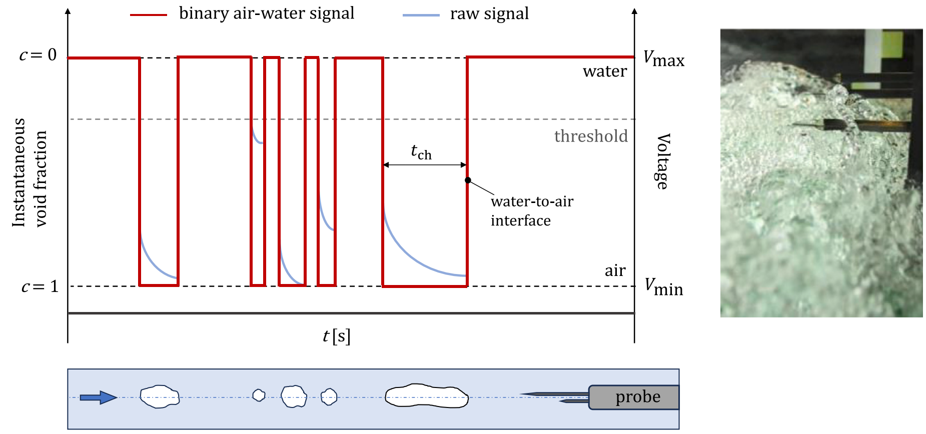

Fig. 2. (left) Sketch of signal processing captured by a probe-tip, using single threshold technique, set at 80%.; (right) Picture of probe set-up (picture by D. Wüthrich).

Previous studies commonly used a threshold value of 50%, i.e. $V_T = 0.5 \cdot (V_{max} + V_{min})$ (Wang, 2014; Bai et al., 2016; Wüthrich et al., 2022b); however, most of these studies focused on steady flows (e.g., hydraulic jumps and spillways). The unsteady flow behavior in dam-break waves and its 3D motions can result in more incomplete piercings as the wave passes the tips (Hohermuth et al., 2021; Shi et al., 2023c). Wüthrich and Regout (2024) conducted a sensitivity study comparing a range of threshold values from 10 to 95%, demonstrating that higher values tend to be more suitable for dam-break waves. Based on these results, this study applied a single threshold technique with a value of 80%.

As shown in Fig. 2, the binarized signal contains information on the number of interfaces from air-to-water or water-to-air, their distribution over time, and the duration between two distinct transitions. These signals are analyzed using statistical tools and all repetitions were synchronized at $t = 0$ s based on the first air-to-water interface detected by the right tip of the reference probe. Results were then ensemble averaged across all repetitions collected at each elevation, in line with Leng and Chanson (2019) and Wüthrich et al. (2022a). Accordingly, the following characteristic air–water flow parameters are obtained:

Number of interfaces: an interface is defined as the transition between air to water, or water to air. Representing the surface boundaries of pierced air bubbles (Fig. 2), the number of interfaces relates to the number of bubbles and water droplets within the roller. When positioned above h_0, the probes are initially in air, causing the first transition to be from air to water as the wave arrives. For measurements at $z > h_0$, the recorded number of bubbles, b, is calculated as $(N\text{-}1)/2$, while $b = N/2$ for measurements at $z < h_0$.

Bubble chord time, and pseudo-chord length: the bubble chord time t_{ch} is defined as the time interval between two successive water-to-air and air-to-water interfaces, which, if pierced at the bubble center, corresponds to the bubble's individual maximum chord time (Fig. 2). Based on t_{ch}, the pseudo-chord length L_{ch} is defined as a characteristic length-scale of the bubbles, and computed as:

$$L_{ch} = t_{ch} \cdot U, \tag{1}$$

where U is the wavefront celerity.

Void fraction: the void fraction $C(x, z, t)$ represents the probability of air being present at a specific position (x, z) and time t, and is a key parameter in multi-phase flow studies (Shi et al., 2021). To compute the void fraction, each binarized instantaneous void fraction signal $c(t)$ is treated as a Bernoulli variable (air = 1 and water = 0). The multiple repetitions at each elevation z are then ensemble-averaged to estimate the likelihood of air presence at (z, t), resulting in the void fraction being defined as:

$$C(z, t) = \frac{n_{c(t)=1}}{n}, \tag{2}$$

where $n_{c(t)=1}$ is the number of times air is detected by a probe-tip, and n is the total number of repetitions.

4. Visual observations

The sudden opening of the gate causes the water volume in the upstream reservoir to collapse as a plunging jet under the influence of gravity, where the induced velocity shear between the wavefront and the still water level initiates the propagating rolling motion and air entrainment (Lubin et al., 2019). The wavefront features a breaking roller characterized by a turbulent air–water mixture with strong recirculation. Fig. 3 illustrates the breaking rollers of dam-break waves for different Froude numbers, propagating over a wet bed. The highly turbulent behavior is evident for all flow conditions, visualized by the large free-surface deformations and vortical structures. Fluctuations and collisions of adjacent vortices lead to air entrapment and de-aeration processes at the surface, resulting in the formation of numerous recurring, rapidly evolving foamy free-surface structures, along with droplets, splashes, air pockets, and bubble clusters (Wüthrich et al., 2021). Moreover, the recirculating motion continuously entrains air into the wavefront at the 'roller toe', marking the sudden discontinuity between the sloping front and the still water level downstream (see Fig. 3). Here, the entrapped air pockets are further broken up into smaller bubbles within the developing shear layer induced by the velocity gradient. The velocity shear initiates large-scale turbulent structures associated with Kelvin–Helmholtz instabilities, which propagate downstream along with the bubbles where they eventually dissipate, and the entrained bubbles rise due to buoyancy (Leng and Chanson, 2019; Wüthrich et al., 2021). The vortical structures at the lower boundary of the shear layer, as shown in Fig. 3, are more visible for FC3 and FC4. This increased visibility of the spatial development of the shear layer over the depth is related to the increase in initial water levels, which in turn are associated with lower Froude numbers and higher Reynolds numbers (Table 2).

5. Free-surface characteristics of dam-break waves

The free surface behavior is quantified in terms of wave surface profiles and wavefront celerity. Herein, changes in water level were measured by the ADMs, with multiple repetitions synchronized, considering $t = 0$s based on the arrival at the corresponding ADM. The wave's hydrodynamic characteristics are analyzed for each condition, using ensemble-statistical methods based on 220 repetitions. Fig. 4 presents the median free-surface water levels obtained by ADM1 ($x/d_0 = 11.68$) and ADM4 ($x/d_0 = 16.68$) for all four flow conditions (see Fig. 1a), along with the standard deviation of ADM4. As similar profiles are obtained by the different ADMs, the dam-break waves appear as fully developed (Stoker, 1957). The largest fluctuations are found at the wavefront, indicated by the broader standard deviation of ADM4. Both the slope steepness and the fluctuations decrease with time,

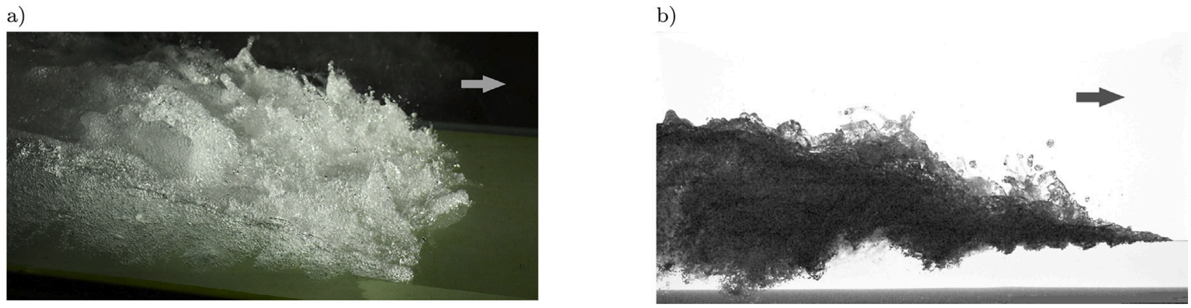

Fig. 3. Side views of air entrainment in dam-break waves propagating over initial still water levels for (a) FC3 [Fr = 2.83; Re = 2.63 $\cdot 10^5$; d_0 = 0.8 m; h_0 = 0.096 m] captured with a DSLR camera (picture by Davide Wüthrich), and (b) FC4 [Fr = 2.44; Re = 3.49 $\cdot 10^5$; d_0 = 0.8 m; h_0 = 0.128 m] captured with a high-speed video camera (16,000 fps).

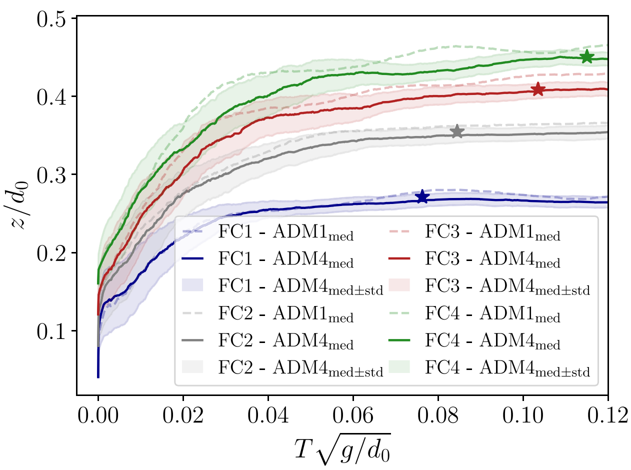

Fig. 4. Comparison of free surface profiles obtained from ADM data for flow conditions FC1 to FC4 [Fr = 5.14–2.44; Re = 0.92 $\cdot 10^5$ - 3.49 $\cdot 10^5$; d_0 = 0.8 m; h_0 = 0.032–0.128 m]. Lines represent the median over 220 reps, while the shaded area is the ± st.dev. The starred markers indicate the end of the roller and the beginning of the plateau height h_p.

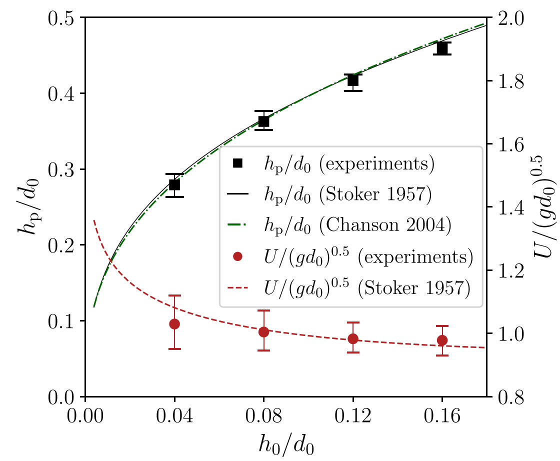

Fig. 5. Comparison of normalized celerity U and plateau height h_p with the analytical expression by Stoker (1957) and empirical expression by Chanson (2004a) for flow conditions FC1–FC4 [Fr = 5.14–2.44; Re = 0.92 $\cdot 10^5$ - 3.49 $\cdot 10^5$; d_0 = 0.8 m; h_0 = 0.032–0.128 m].

resulting in a more constant water level after the wavefront, known as the plateau height h_p. Comparing the different flow conditions, the plateau height increases with higher tailwater depths, accompanied by a steeper slope. These findings are consistent with previous studies on dam-break wave characteristics (Nielsen et al., 2022; Ozmen-Cagatay and Kocaman, 2010; Yang et al., 2022). Fig. 5 displays the influence of tailwater depth on hydrodynamic characteristics, comparing them with analytical expressions by Stoker (1957) and Chanson (2004a). The median plateau height (h_p) and median celerity (U) are shown, with error bars representing the 25%–75% quartiles from 220 repetitions. As h_0 increases, the plateau height rises while the celerity decreases due to increased frictional effects from the higher initial water level. These trends closely align with existing formulations, confirming that the experimental setup accurately reproduces dam-break waves.

6. Air–water flow properties

Visual observations showed large amounts of entrained/entrapped air at the front. This section examines the air–water flow properties under various flow conditions to analyze the relation between air distribution and the hydrodynamic characteristics of dam-break waves. Based on ensemble statistics, the air–water flow properties are quantified in terms of the number of interfaces (Section 6.1), bubble characteristics (Section 6.2), and the void fraction (Section 6.3). First, general tendencies of these properties in the vertical direction are addressed, followed by a comparison across different flow conditions. Fig. 4 shows variations in plateau height h_p across different flow conditions. To enable meaningful comparison, a normalized elevation $h^*(z)$ is introduced as:

$$h^*(z) = \frac{z - h_0}{h_p - h_0}, \tag{3}$$

where z is the elevation (with $z = 0$ representing the bottom of the flume), h_0 is the tailwater depth, and h_p is the plateau height. This normalization sets $h^*(z = h_0) = 0$ and $h^*(z = h_p) = 1$, allowing comparison across the relative height of the aerated roller, which includes 13 elevations per flow condition, within the range of $-0.05 < h^* < 0.94$.

6.1. Number of interfaces

The phase change detected by a single probe-tip, defined as an interface, indicates a transition from water to air or vice versa. Fig. 6a,b show the number of interfaces N at normalized elevations h^* for FC1 (Fr = 5.14) and FC3 (Fr = 2.83), respectively. The boxplot displays the statistical distribution, including the median, spread, and skewness, based on 55 repetitions for each elevation, except the reference probe, which uses 220 repetitions. The box extends from the 25th to the 75th percentile, with a vertical line inside representing the ensemble median (50th percentile). The whiskers extend to the lowest or highest number of interfaces, excluding any outliers. As shown in Fig. 6a,b, the number of interfaces increases for $h^* > 0$, reaching a local maximum, and then decreases for higher h^* values, forming an S-shaped curve, particularly evident at higher Froude numbers (FC1). A local maximum was observed at $h^* \sim [0.13 - 0.3]$ for all flow conditions, slightly above the initial water level ($h^* = 0$), indicating similarities with

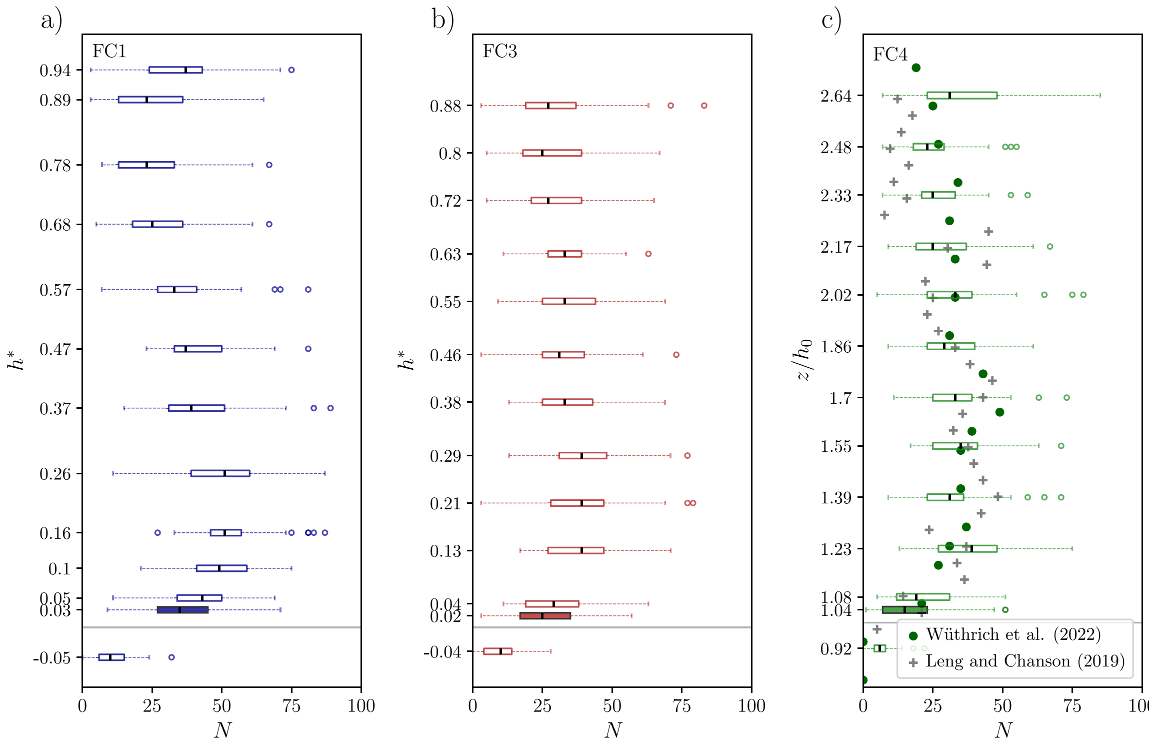

Fig. 6. Boxplots of the number of interfaces N across normalized elevations h^* for (a) FC1 [Fr = 5.14; Re = 0.92 $\cdot 10^5$; d_0 = 0.8 m; h_0 = 0.032 m], and (b) FC3 [Fr = 2.83; Re = 2.63 $\cdot 10^5$; d_0 = 0.8 m; h_0 = 0.096 m]. (c) Boxplot of the number of interfaces N for FC4 [Fr = 2.44; Re = 3.49 $\cdot 10^5$; d_0 = 0.8 m; h_0 = 0.128 m] compared with median N of breaking bore studies by Wüthrich et al. (2022a) [Fr = 2.4, Re = $1.32 \cdot 10^5$], and Leng and Chanson (2019) [Fr = 2.1, Re = $2.06 \cdot 10^5$] at normalized elevations z/h_0 (note that in both previous studies Fr = $(V_1 + U)/\sqrt{gh_0}$, where V_1 is the velocity of the initial flow). The reference probe measurements (based on 220 tests) are indicated by the highlighted boxes. The gray lines indicate the initial water level.

steady hydraulic jumps (Wang, 2014; Wüthrich et al., 2022b). These observations confirm the presence of a shear layer in dam-break waves. A slight increase in N was detected in the upper part of the roller for FC1, likely due to free surface fluctuations.

Fig. 6c compares the results of FC4 (Fr = 2.44) with the experimental data of Wüthrich et al. (2022a) and Leng and Chanson (2019), who analyzed air–water flow properties in breaking bores with similar Froude numbers (Fr = 2.4 with Re = $1.32 \cdot 10^5$, and Fr = 2.1 with Re = $2.06 \cdot 10^5$), albeit propagating on an initial flow with non zero velocities. Note that the comparison of FC4 with the ensemble-median number of interfaces $\langle N \rangle$ from previous studies is presented for normalized elevations z/h_0, due to differences in the experimental set-up. The results from Wüthrich et al. (2022a) are similar to the present study, though they did not observe bubbles below the initial water level and reported a higher maximum number of interfaces ($\langle N \rangle_{max}$ = 49 at $z/h_0 = 1.65$). The results of Leng and Chanson (2019) are also comparable to the other datasets, with $\langle N \rangle_{max}$ = 48.33 at $z/h_0 = 1.4$. However, their distribution exhibits greater scatter, likely due to fewer repetitions, highlighting the importance of repetition for statistically reliable results. Variations in $\langle N \rangle_{max}$ compared to the previous studies can be attributed to differences in Reynolds numbers, as discussed by Estrella et al. (2022b). Additionally, Montano and Felder (2018) found that bubble count rates were higher in hydraulic jumps with a fully developed boundary layer compared to a partially developed boundary layer. The generally lower median number of interfaces in FC4 compared to the breaking bores may therefore be attributed to differences in inflow conditions affecting the presence of a fully developed boundary layer. Despite this, the results showed consistency with previous studies both quantitatively and qualitatively.

Fig. 7a presents the ensemble-median number of interfaces $\langle N \rangle$ of all four flow conditions FC1 to FC4. While the local maximum occurs at a similar relative elevation $[0.13 < h^* < 0.3]$, its magnitude varies among the different flow conditions. Specifically, $\langle N \rangle_{max}$ = 51 for Fr = 5.14, whereas $\langle N \rangle_{max}$ = 38 for Fr = 2.44. This increasing trend of $\langle N \rangle_{max}$ with increasing Froude number is most visible in the shear layer, supported by similar findings in hydraulic jumps (Wang, 2014; Wüthrich et al., 2022b). This is emphasized in Fig. 7b, depicting an increasing behavior of $\langle N \rangle_{max}$ for higher Froude numbers. Differences for Fr< 3 compared to $\langle N \rangle_{max}$ in previous studies likely stem from variations in Reynolds numbers and the presence of a (partially) developed boundary layer, as discussed earlier. In the upper part of the aerated roller, also called the recirculation zone, the influence of the Froude number on $\langle N \rangle$ is less pronounced, with local minima ranging between $20 < \langle N \rangle_{min} < 25$. Fig. 7a clearly shows that for FC1 the difference in the number of interfaces between the shear layer and the recirculation zone is more than double, indicating much stronger variations in $\langle N \rangle$ with depth compared to the other flow conditions. This suggests that variations in Froude number have the strongest effect on the number of interfaces in the shear layer. This is consistent with findings in hydraulic jumps, demonstrating similarities between steady and unsteady flows.

6.2. Bubble characteristics

The presence of air influences many dynamic flow processes, where not only the number of bubbles, but also their size play an important role. The exposure time of the probe-tip to air determines the bubble's chord time t_{ch} (Section 3). Due to the highly transient nature of dam-break waves, bubble characteristics evolve spatially and temporally, as shown in Fig. 8 for flow condition FC1 (Fr = 5.14), offering simultaneous insight into the variations in both dimensions. Here, Fig. 8a depicts the ensemble-median free-surface profile of ADM 4, along with its fluctuations (± std.dev.). The variations in bubble characteristics over time are shown for four distinct time intervals, shaded in gray, with corresponding subplots presented in Fig. 8b. Each subplot shows the probability of occurrence of bubble-chord time t_{ch} at elevation h^*,

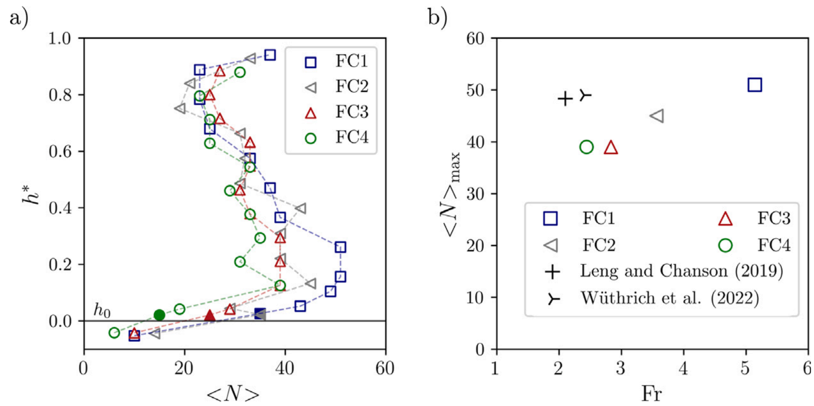

Fig. 7. (a) Comparison of the ensemble-median number of interfaces $\langle N \rangle$ across normalized elevations h^* for flow conditions FC1–FC4 [Fr = 5.14–2.44; Re = 0.92 $\cdot 10^5$ - 3.49 $\cdot 10^5$; d_0 = 0.8 m; h_0 = 0.032 - 0.128 m]. Reference probe measurements (based on 220 tests) are indicated by the full markers. (b) Comparison of $\langle N \rangle_{\max}$ of FC1–FC4 [Fr = 5.14–2.44; Re = 0.92 $\cdot 10^5$ - 3.49 $\cdot 10^5$; d_0 = 0.8 m; h_0 = 0.032–0.128 m] with experimental data of Leng and Chanson (2019) [Fr = 2.1, Re = 2.06 $\cdot 10^5$] and Wüthrich et al. (2022a) [Fr = 2.4, Re = 1.32 $\cdot 10^5$].

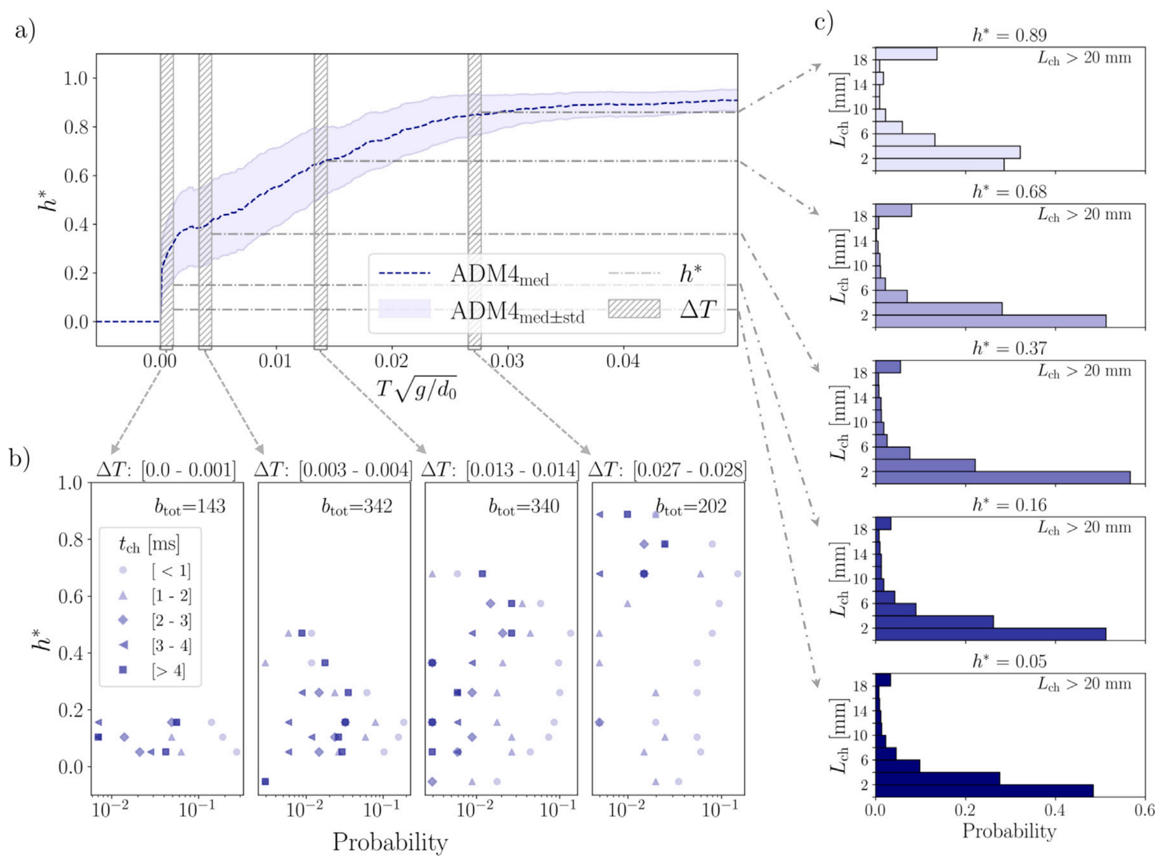

Fig. 8. Spatial and temporal variations of the bubble characteristics for FC1 [Fr = 5.14; Re = 0.92 $\cdot 10^5$; d_0 = 0.8 m; h_0 = 0.032 m]: (a) the ensemble-median free-surface profile and fluctuations obtained with ADM4. (b) the probability of occurrence of bubble-chord time t_{ch} at elevation h^*, indicated with different markers, based on the total number of bubbles b_{tot} recorded over 55 repetitions within the associated time interval ΔT. (c) PDF distributions of L_{ch} (Eq. (1)) at 5 selected elevations h^*.

indicated with different markers, based on the total (cumulative) number of bubbles b_{tot} recorded over 55 repetitions within the associated time interval ΔT. Furthermore, Fig. 8c displays horizontally oriented probability density functions (PDF) of the pseudo-chord length $L_{\text{ch}} = U \cdot t_{\text{ch}}$ at 5 selected elevations within the aerated zone, indicated by the horizontal dashed lines in Fig. 8a.

The PDFs in Fig. 8c show strongly skewed curves, indicating that mostly small bubbles are detected, with approximately 80% having $L_{\text{ch}} < 6$ mm at most elevations. The probability P($L_{\text{ch}} < 2$ mm) increases for $h^* > 0$, reaching a local maximum before decreasing in the upper part of the roller. This suggests that smaller bubbles are more prevalent at lower elevations within the shear layer. Despite some large outliers observed for L_{ch} >20 mm, likely due to surface fluctuations, the local skew towards larger L_{ch} values at higher elevations implies larger bubbles are found in the recirculation zone. These L_{ch} variations with depth correspond to the variations in the number of interfaces, where peaks in small bubble probability align with local maxima in the number of interfaces (Fig. 6). Comparable with the PDFs, each time interval in Fig. 8b shows the highest probability for $t_{\text{ch}} < 1$ ms at all elevations. However, initially, higher probabilities appear for larger

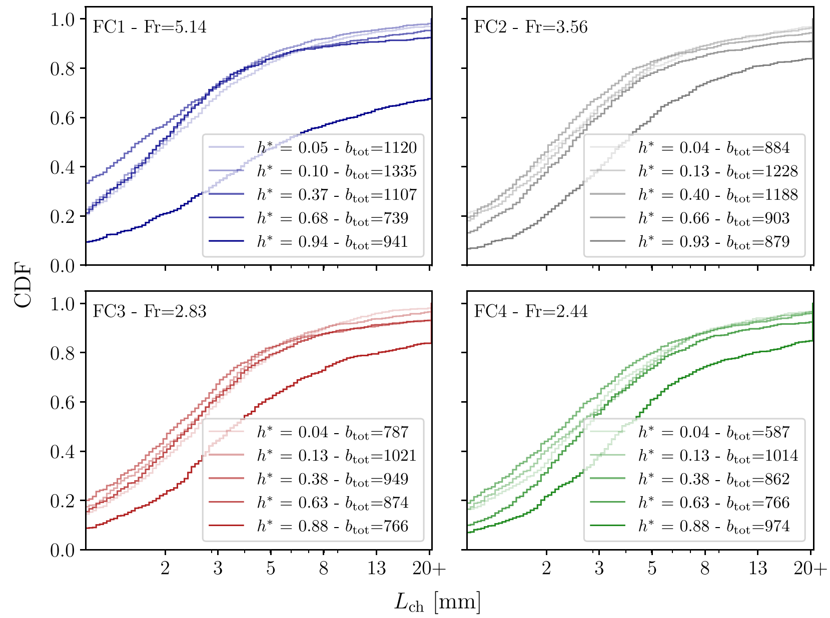

Fig. 9. Comparison of CDF distributions of pseudo-chord length $L_{\rm ch}$ [mm] at selected elevations for flow conditions FC1–FC4 [Fr = 5.14–2.44; Re = 0.92 $\cdot 10^5$–3.49 $\cdot 10^5$; d_0 = 0.8 m; h_0 = 0.032–0.128 m], based on the total number of bubbles $b_{\rm tot}$ recorded over 55 repetitions at each elevation.

bubbles (i.e., $t_{\rm ch} > 4$ ms) at each elevation, while only smaller bubbles are recorded as time progresses. This pattern indicates that larger bubbles accumulate near the wavefront surface and diminish deeper into the wave. Hence, the spatial and temporal variations in bubble characteristics quantitatively support the observed physical processes (Section 4); with strong air–water interactions at the turbulent roller's free surface and larger air pockets trapped at the roller toe, which are broken down by turbulent shear layer processes until buoyancy forces them to rise within the recirculation zone.

Fig. 9 compares cumulative density function (CDFs) of pseudo-chord length ($L_{\rm ch}$) at five selected elevations, to investigate bubble characteristics across the different flow conditions. Each flow condition exhibits right-skewed distributions, with steeper curves typically observed at lower elevations, indicating higher probabilities for smaller bubble sizes. At $h^* \sim 0.38$, the highest cumulative probability for $L_{\rm ch} > 2$ mm ranges from 40% for FC4 (Fr = 2.44) to almost 60% for FC1 (Fr = 5.14). The mildest slope is observed at the highest elevation, $h^* \sim 0.9$, which can be attributed to free-surface fluctuations. In this regard, FC1 exhibits the greatest deviation over depth, with the steepest slope at lower elevations and the mildest slope at the highest elevation compared to other flow conditions. Lower Froude numbers display more dispersed CDF curves with milder slopes, suggesting a wider range of larger bubbles. This behavior, with the strongest deviations observed at the highest Froude number, reflects the effects of changes in the Froude number on the number of interfaces found in Section 6.1. Hence, it supports the strong relation between hydrodynamic characteristics and the degree of fragmentation in terms of bubble quantity and size.

Both the quantity and characteristics of bubbles influence the air concentration in the wavefront. To compare these properties together among different flow conditions, Fig. 10a visualizes $t_{\rm ch}$ across the normalized elevations, with different markers indicating the corresponding range in number of interfaces at h^*. Median values of the bubble-chord time $t_{\rm ch,med}$ and number of interfaces $\langle N \rangle$ were used to mitigate the influence of extreme outliers (Chanson, 2020). Due to the prevalent skewness towards smaller bubbles in all conditions (Fig. 9), $t_{\rm ch,med}$ typically remains below 2 ms. While differences may seem subtle, several correlations between the properties can be observed. For each flow condition, the lowest $t_{\rm ch,med}$ values coincide with maximum $\langle N \rangle$ values, consistently observed at elevations from $0.1 < h^* < 0.35$, corresponding to the shear layer. In contrast, larger $t_{\rm ch,med}$ values align with lower values of $\langle N \rangle$ in the recirculating zone. As higher $t_{\rm ch}$ values become more dispersed throughout the depth for decreasing Fr, larger bubbles are generally found for lower Froude numbers. Subsequently, Fig. 10b compares the influence of more, smaller bubbles versus fewer, larger bubbles on the total amount of air present. The product of the median pseudo-chord length and the median number of bubbles at each elevation serves as an indicator of air volume variations across different heights. Up to $h^* \approx 0.15$, variations between the different flow conditions appear minimal, suggesting that the air volume remains similar despite different combinations in quantity and size shown in Fig. 10a. FC1 shows a more pronounced S-curve profile, indicating that air is locally concentrated at lower elevations, while it appears more evenly distributed across the height for other flow conditions. However, these conditions are also associated with lower celerity, highlighting the complex interplay between spatial and temporal factors in unsteady flows.

6.3. Void fraction

The ensemble-averaged void fraction $C(z,t)$, defined by Eq. (2), quantifies the air content in the wavefront by indicating the likelihood of air presence at a specific time and location. With similar results found for all flow conditions, Fig. 11a shows a contour plot for FC2, displaying varying C values based on 55 repetitions at each elevation. Herein, the z_{90} curve is introduced, marking the elevation where $C(z,t) = 0.9$, serving as a definition of the free-surface level. Overall, the contour plot clearly illustrates that the highest aeration levels are located slightly below the free surface, showing a decreasing trend with time. Higher values of C are locally observed within the range of $0.05 < h^* < 0.3$, consistent with elevations where local maxima of the number of interfaces were detected. This further confirms the presence of a shear layer, situated just above the tailwater depth h_0, which was consistently observed for all flow conditions.

Given the highly transient behavior in space and time, both depth-dependent and time-dependent parameters are introduced to compare the void fraction across different flow conditions. For every time instance t, the depth-averaged void fraction $C_{{\rm mean},z}$ is obtained by integrating C over the depth from $z = 0$ to $z = z_{90}$:

$$C_{{\rm mean},z}(t) = \frac{1}{z_{90}} \int_{z=0}^{z=z_{90}} C(z,t)\,{\rm d}z\,. \tag{4}$$

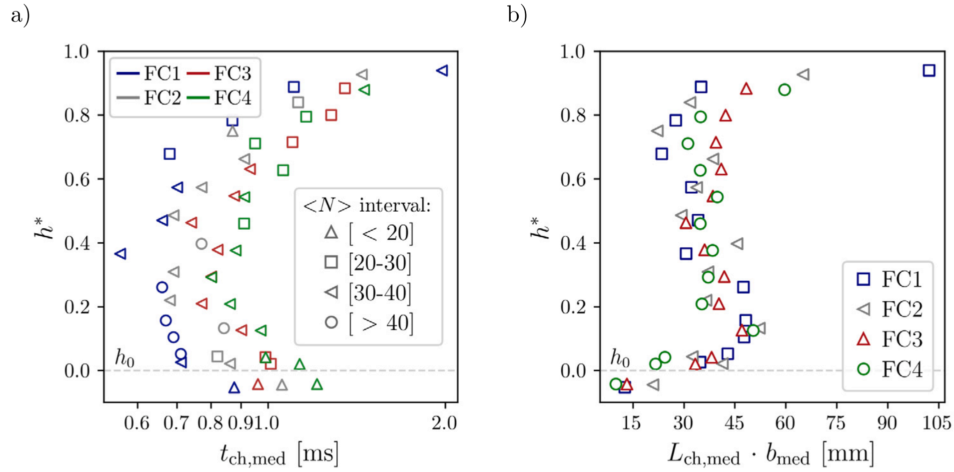

Fig. 10. (a) Comparison of $t_{\mathrm{ch,med}}$ across normalized elevations h^* for flow conditions FC1–FC4 [Fr = 5.14–2.44; Re = 0.92 $\cdot 10^5$–3.49 $\cdot 10^5$; d_0 = 0.8 m; h_0 = 0.032–0.128 m], with the corresponding values for $\langle N \rangle$ at each elevation indicated by the different markers. Different colors represent different flow conditions. (b) Comparison of pseudo air volume $L_{\mathrm{ch,med}} \cdot b_{\mathrm{med}}$ across normalized elevations h^* for flow conditions FC1–FC4 [Fr = 5.14–2.44; Re = 0.92 $\cdot 10^5$–3.49 $\cdot 10^5$; d_0 = 0.8 m; h_0 = 0.032–0.128 m]. With $L_{\mathrm{ch,med}}$ the median pseudo-chord length, and b_{med} the median number of bubbles recorded at corresponding elevation h^*.

Similarly, for each elevation z, the time-averaged void fraction $C_{\mathrm{mean},t}$ is obtained by integrating C over time from $t = t_0$ to $t = t_{\max}$, with t_0 being the time when $z = z_{90}$, and $t_{\max}$ the maximum time instance obtained for z_{90}, i.e., where z_{90} reaches its maximum elevation ($z_{90} \sim h_p$):

$$C_{\mathrm{mean},t}(z) = \frac{1}{t_{\max}} \int_{t=t_0}^{t=t_{\max}} C(z,t)\,\mathrm{d}t \tag{5}$$

Fig. 11c illustrates $C_{\mathrm{mean},z}$ over time for all flow conditions, revealing an increasing trend within the range $0 < T\sqrt{g/d_0} < 0.25$. However, the magnitude of the maximum $C_{\mathrm{mean},z}$ varies significantly among flow conditions, with FC1 (Fr = 5.14) reaching a peak of approximately 0.39, nearly double the maximum of FC4 (Fr = 2.44), i.e., $C_{\mathrm{mean},z} \approx 0.23$. Furthermore, $(C_{\mathrm{mean},z})_{\max}$ of FC1 occurs more rapidly compared to the other flow conditions, where the increase is more gradual. For $T\sqrt{g/d_0} > 0.25$, a decreasing trend is observed for all flow conditions, stabilizing at $C_{\mathrm{mean},z} \approx 0.10$ in the tail of the wavefront. Interestingly, the maximum values appear to follow an increasing behavior for higher Fr, as shown in Fig. 11d, which presents the $(C_{\mathrm{mean},z})_{\max}$ of all FCs. Here, the maximum values of the depth-averaged void fraction are also compared with previous data from Wüthrich et al. (2022a) (Fr = 2.4) and Leng and Chanson (2019) (Fr = 2.1) for bores propagating on a non-still initial water level, along with data from hydraulic jump studies by Wang (2014) (Fr = 3.8, 5.1) and Estrella et al. (2022b) (Fr = 2.1). While the data align with previous studies, dam-break waves show a higher maximum air concentration than hydraulic jumps for higher Froude numbers. This discrepancy may result from the unsteady nature of the flow, which enhances velocity shear and increases air entrainment in the roller, while differences in signal processing of unsteady flows could also contribute. As measurements in hydraulic jumps are obtained at selected cross-sections along the roller, it is possible that the discrete nature of these localized measurements may not capture the maximum values. Finally, Fig. 11b compares the time-averaged void fraction, representing the average air concentration over height by averaging instantaneous void fraction profiles across all time instances. The results show a similar increasing trend up to $h^* < 0.3$, indicating that roughly 25% of the air concentration is located in the lower part of the wave for all flow conditions. The gradients of the curves from FC2 to FC4 flatten at higher elevations. Comparing this with the contour plot visualization (see Fig. 11a for FC2), aerated area of the roller, i.e., the distance between z_{90} and z_{10}, remains relatively constant across all flow conditions but increases from FC2 to FC4 at higher elevations.

7. Application of advection–diffusion models to dam-break waves

Results on key air–water flow properties indicate that an increase in Froude number enhances the bubble-breaking process, leading to a greater number of smaller bubbles in the shear layer and more pronounced variations in bubble quantity and size with depth. Previous research on (steady) multiphase flows has categorized the spatial and temporal behavior of air into different regions based on distinct driving mechanisms, as discussed in Section 4 (Murzyn et al., 2005; Chanson, 2011). Various advection–diffusion models have been developed to define the void fraction at normalized distances from the roller toe, which are summarized in Table 3 and Fig. 12. While the steady nature of hydraulic jumps allows for direct analysis in a Lagrangian reference frame, the unsteadiness of dam-break waves first requires converting time-dependent air–water flow properties into an equivalent distance across the breaking roller. A roller length definition is therefore introduced based on the geometric characteristics of the free-surface, analogous to hydraulic jumps, where this length is typically defined as the longitudinal distance over which water elevation increases monotonically (Wang, 2014). Consequently, the roller length is computed as $L_r = U \cdot T_r$, where U represents the wavefront celerity, and T_r the duration for the sloping wavefront to reach the plateau height h_p, as indicated by the markers in Fig. 4. Hence, the following roller lengths are obtained with L_r/h_0 = 62.0, 33.6, 26.8, 22.26 for FC1 to FC4, respectively.

Fig. 13 presents four instantaneous ensemble-averaged void fraction profiles for each flow condition, compared with analytical models across the roller. For $TU/L_r \lesssim 0.01$, immediately downstream of the roller toe, entrained air pockets are primarily influenced by buoyancy, drag, and gravitational forces, resulting in a void fraction profile with a convex shape, well represented by Eq. 6 (Shi et al., 2023a), as shown in the first column of Fig. 13. In addition to distinct regions described in previous studies, the experimental data from dam-break waves show a transition phase for $0.01 \lesssim TU/L_r \lesssim 0.09$ (second column in Fig. 13). Here, air bubbles begin to interact with turbulent flow structures, however, a fully developed shear layer is not yet visible. The profiles evolve from a convex to an S-shape, aligning with the error function described by Eq. 7 (Chanson, 1989), across the entire water column. At some distance from the toe ($0.09 \lesssim TU/L_r \lesssim 0.3$), the void fraction exhibits a characteristic shape similar to hydraulic jumps, with the roller separating into a lower shear layer and an upper recirculation zone. In the shear layer, turbulence dominates, breaking up air bubbles and advecting them downstream within vortex

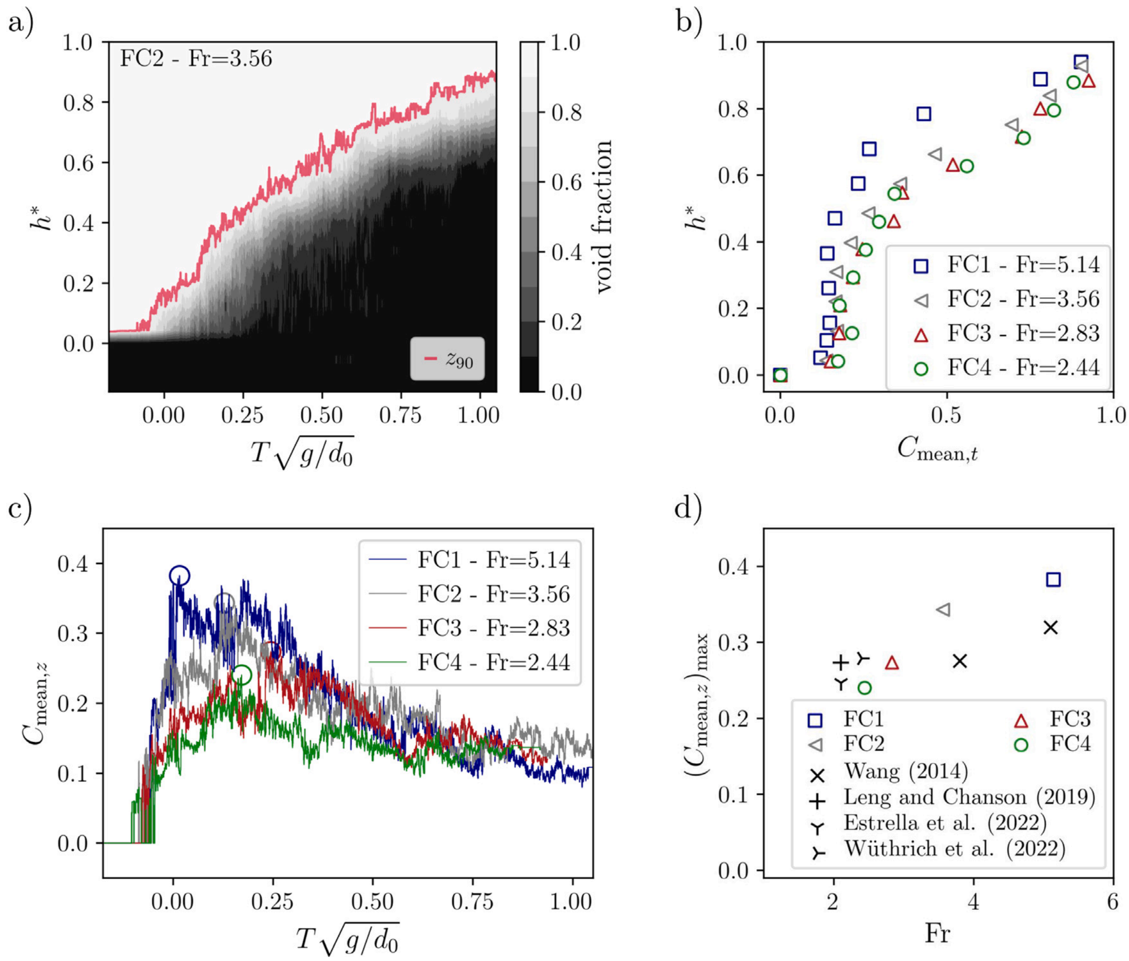

Fig. 11. (a) Contour plot of ensemble-averaged instantaneous void fraction $C(z,t)$ for FC2 [Fr = 3.56, Re = 1.8 $\cdot 10^5$; d_0 = 0.8 m; h_0 = 0.064 m]. (b) Comparison of the time-averaged void fraction $C_{\mathrm{mean},t}$ for flow conditions FC1–FC4 [Fr = 5.14–2.44; Re = 0.92 $\cdot 10^5$–3.49 $\cdot 10^5$; d_0 = 0.8 m; h_0 = 0.032–0.128 m]. (c) Comparison of the depth-averaged void fraction $C_{\mathrm{mean},z}$ for flow conditions FC1–FC4 [Fr = 5.14–2.44; Re = 0.92 $\cdot 10^5$–3.49 $\cdot 10^5$; d_0 = 0.8 m; h_0 = 0.032–0.128 m]. (d) Comparison of the maximum values of $C_{\mathrm{mean},z}$ of FC1–FC4 [Fr = 5.14–2.44; Re = 0.92 $\cdot 10^5$–3.49 $\cdot 10^5$; d_0 = 0.8 m; h_0 = 0.032–0.128 m] with data of breaking bores studies by Leng and Chanson (2019) [Fr = 2.1, Re = 2.06$\cdot 10^5$], Wüthrich et al. (2022a) [Fr = 2.4, Re = 1.32$\cdot 10^5$], and hydraulic jump studies by Wang (2014) [Fr = 3.8, Re = 1.6$\cdot 10^5$; Fr = 5.1, Re = 0.91$\cdot 10^5$], and Estrella et al. (2022b) [Fr = 2.1, Re = 3.05$\cdot 10^5$].

structures. This is reflected in a local maximum, $C_{\max}$, which initially increases and then gradually decreases as air diffuses, leading to shear layer dissipation around $TU/L_r \sim 0.3$. The experimental data aligns well with the exponential function in Eq. 8 (Chanson, 1995). The recirculation zone near the free surface is characterized by recirculating motions and dynamics dominated by gravitational forces, represented by an S-curve in the void fraction profile. This region shows a rapid increase of C towards the upper part, following the error function defined by Chanson (1989). The agreement between the experimental data and these models aligns with findings from studies on hydraulic jumps (Wang, 2014; Murzyn et al., 2005; Chachereau and Chanson, 2011a) and breaking bores (Shi et al., 2023a; Wüthrich et al., 2022a), albeit (Wüthrich et al., 2022a) noted the absence of a clearly defined shear layer in their data. Ultimately, for $TU/L_r \gtrsim 0.3$, the air is diffused to the point where the shear layer dissipates, and the void fraction profile once again aligns well with Eq. 7 across the entire water column.

The advection–diffusion coefficients, D^* and $D^\#$ in Eq. 7 and 8, were derived from the best-fit analysis of the data, and they are key parameters in air diffusion models, indicating the change in diffusivity across the aerated regions. Accordingly, the diffusivity coefficients are illustrated in Fig. 14, compared with previous studies on hydraulic jumps conducted by Chachereau and Chanson (2011a) and Wang (2014). Here, the shaded area for $TU/L_r \lesssim 0.09$ indicates the part of the roller where the shear layer is not developed. For $TU/L_r \gtrsim 0.09$, $D^\#$ increases and D^* decreases with distance from the roller toe, consistent with trends observed in previous hydraulic jump studies. The shear coefficient $D^\#$ exhibits higher variability, likely due to the unsteady nature of the flow, hindering precise fitting of the scattered data, despite the presence of a visible shear layer found in all flow conditions. Variations in $D^\#$ in comparison to previous hydraulic jump studies may arise from the presence of a (partially) developed boundary layer, a factor similarly discussed in relation to the number of interfaces. This may affect the magnitude of the diffusivity in the shear layer as Montano and Felder (2018) showed higher void fractions in the

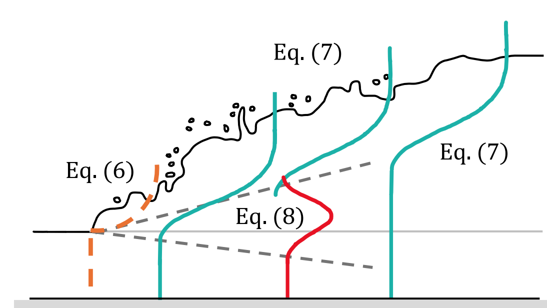

Fig. 12. Sketch of analytical models of air diffusion along the roller.

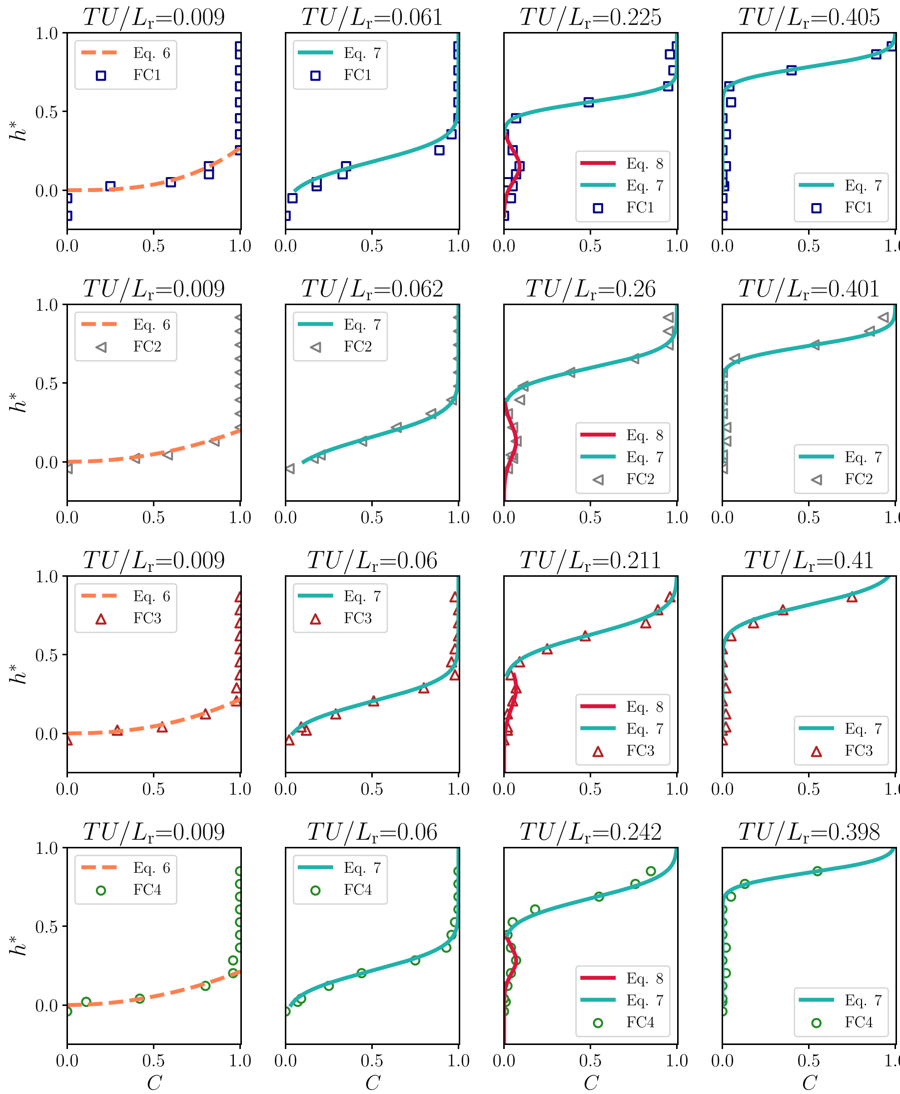

Fig. 13. Comparison of void fraction C profiles across normalized elevations h^* between the experimental data and solutions of different analytical models (see Table 3) for flow conditions FC1–FC4 [U = 2.88–2.73 m/s; Fr = 5.14–2.44; Re = 0.92 $\cdot 10^5$–3.49 $\cdot 10^5$; d_0 = 0.8 m; h_0 = 0.032–0.128 m].

Table 3
Summary of analytical models of air diffusion in different regions.

air diffusion model at the toe of wavefront (Shi et al., 2023a)		
$C(z,t) = 0.9\left(\frac{z-h_0}{z_{90}-h_0}\right)^M$ $M = \frac{0.9}{C_{\mathrm{mean},z}} - 1$	$0 < z < z_{90}$	(6)
air diffusion model in recirculation zone (Chanson, 1989)		
$C(z,t) = \frac{1}{2}\left(1 + \mathrm{erf}\left(\frac{z - z_{50}}{2\sqrt{D^* \cdot t}}\right)\right)$	$z^* < z$	(7)
air diffusion model in the shear layer (Chanson, 1995)		
$C(z,t) = C_{\max} \cdot \exp\left(-\frac{1}{4D^\#}\frac{\left(\frac{z-z_{c_{\max}}}{h_0}\right)^2}{\frac{U\cdot t}{h_0}}\right)$	$0 < z < z^*$	(8)

Notes: $C_{\mathrm{mean},z}$ is the depth-averaged void fraction, integrated from $z = h_0$ to $z = z_{90}$; $C_{\max}$ is the local maximum of C in the shear layer, and its corresponding elevation $z_{c_{\max}}$; z_{50} is the elevation for which C = 0.5; z^* is the elevation which defines the transition from the shear layer to the recirculation zone; $D^\#$ and D^* are the diffusivity coefficients in the shear layer and recirculation zone, obtained from the best-fit analysis of the data.

shear region for hydraulic jumps with fully developed boundary layers. Finally, resulting from the probe set-up used herein, the recirculating behavior induces air movements opposite to the probe orientation in the recirculation zone (Fig. 1), while the convective air transport in the shear layer aligns with the probe orientation. This orientation discrepancy for distinct zones differs from previous steady flow studies, such as Wang (2014), which included probe measurements in both directions and may result in a more clearly defined shear layer in hydraulic jump data. Despite this, data showed similarities with the steady hydraulic jumps, showing parallels between steady and unsteady flows.

8. Conclusion

Understanding the turbulent, multiphase nature of highly unsteady flows is crucial for optimizing structural designs and mitigating risks associated with phenomena like tsunamis, impulse waves, and storm surges. For that, of particular interest are dam-break waves over wet bed, where the strong recirculating air–water mixture caused by breaking of the wavefront significantly influences various dynamic processes and wave characteristics. This experimental study quantified air–water

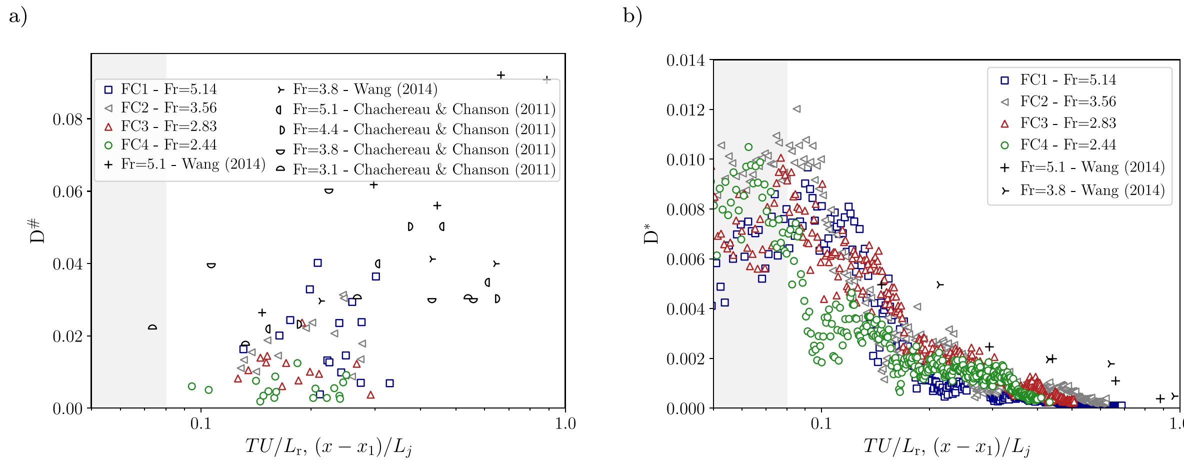

Fig. 14. (a) Comparison of diffusivity coefficient $D^{\#}$ in the shear layer for flow conditions FC1–FC4 [U = 2.88–2.73 m/s; Fr = 5.14–2.44; Re = 0.92 $\cdot 10^5$–3.49 $\cdot 10^5$; d_0 = 0.8 m; h_0 = 0.032–0.128 m], with data from Wang (2014) [Fr = 5.1, Re = 0.91 $\cdot 10^5$; Fr = 3.8, Re = 1.6 $\cdot 10^5$], and Chachereau and Chanson (2011a) [Fr = 5.1, Re = 1.3 $\cdot 10^5$; Fr = 4.4, Re = 1.1 $\cdot 10^5$; Fr = 3.8, Re = 0.98 $\cdot 10^5$; Fr = 3.1, Re = 0.89 $\cdot 10^5$]. (b) Comparison of diffusivity coefficient D^* in the recirculation zone for flow conditions FC1–FC4 [U = 2.88–2.73 m/s; Fr = 5.14–2.44; Re = 0.92 $\cdot 10^5$–3.49 $\cdot 10^5$; d_0 = 0.8 m; h_0 = 0.032–0.128 m], with data from Wang (2014) [Fr = 5.1, Re = 0.91 $\cdot 10^5$; Fr = 3.8, Re = 1.6 $\cdot 10^5$]. The gray shaded area indicates part of the wave where $TU/L_r < 0.09$. L_r is the length of the dam-break roller, while L_j is the roller length of the hydraulic jump.

flow properties using a novel approach, allowing to analyze the unsteady multiphase nature for four flow conditions. Dam-break wave experiments were conducted in a large-size flume using a lift gate. Due to the unsteadiness of the flow, tests were repeated multiple times and data analysis was based on ensemble-averaging techniques to obtain physically meaningful and statistically reliable results. The air–water flow properties were examined in terms of air concentration (void fraction) and bubble characteristics (quantity and size), with these properties compared between the different flow conditions and associated Froude numbers.

Visual observations revealed highly aerated flows, with non-linear, turbulent behavior at the wavefront, characterized by rapidly changing deformations of the free surface, which enhance air entrapment and entrainment, leading to droplets, splashes, air pockets, and clusters of bubbles. Within the breaking roller, large-scale turbulent structures associated with Kelvin–Helmholtz instabilities were visible, which were advected downstream until they eventually dissipated. Dam-break waves with lower Froude numbers showed increased wave heights but reduced celerity compared to waves with higher Froude numbers, due to frictional effects from the greater tailwater depth, consistent with analytical formulations.

The analysis of air–water flow properties consistently reflected the observed dynamic processes. For all flow conditions, a local maximum in the number of bubbles, accompanied by a minimum in bubble size, was found slightly above the initial still water level, aligning with previous findings in (un)steady multiphase flows. The greatest contrast between local maxima and minima was observed in waves with the highest Froude numbers, while larger bubbles were generally found at lower Froude numbers. These results suggest that increasing the Froude number intensifies dynamic processes responsible for bubble fragmentation in the lower part of the roller. The void fraction, a parameter commonly used to represent the likelihood of air concentration, showed similar profiles across the water column for all flow conditions. The maximum depth-averaged void fraction exhibited an increasing trend with higher Froude numbers, reaching air concentrations of up to 40% for Fr = 5.14. Findings on bubble characteristics and void fraction indicated distinct regions across the roller, confirming the presence of a shear layer and recirculation zone in dam-break waves, with void fraction profiles closely matching analytical models developed for steady flows. Slightly downstream of the wave toe, the instantaneous void fraction profiles exhibited a convex shape, followed by an S-shape, after which the shear layer became fully visible - a pattern in the roller not previously documented in studies of similar flow phenomena.

Overall, the high levels of aeration, along with the spatial and temporal variations in air–water properties for different flow conditions, underscore the importance of considering air in dam-break waves. Acknowledging the complexity of these phenomena, the results offer new insights into the relationship between the multiphase nature and the hydrodynamic processes within the breaking roller. Additionally, the study supports this experimental approach for collecting multiphase flow data in highly turbulent, unsteady flows, with broader implications for developing numerical methods to incorporate air entrainment.

9. Notation

b = number of bubbles [–]
b_{med} = median number of bubbles [–]
b_{tot} = total number of bubbles [–]
c = instantaneous void fraction [–]
C = ensemble-averaged void fraction, defined by Eq. (2) [–]
C_{max} = local maximum of C in the shear layer [–]
$C_{mean,t}$ = time averaged void fraction, defined by Eq. (5) [–]
$C_{mean,z}$ = depth averaged void fraction, defined by Eq. (4) [–]
d = inflow depth [m]
d_0 = impoundment depth of reservoir [m]
$D^{\#}$ = diffusivity coefficient in recirculation zone [–]
D^* = diffusivity coefficient in shear layer [–]
Fr = Froude number, defined as Fr= $U/\sqrt{gh_0}$ [–]
g = gravitation acceleration [9.81 ms^{-2}]
h_0 = initial still water level downstream of the gate [m]
h_p = plateau height [m]
h^* = normalized elevation, defined by Eq. (3) [–]
L_{ch} = pseudo-chord length, defined by Eq. (1) [m]
$L_{ch,med}$ = median pseudo-chord length [m]
L_j = roller length in a hydraulic jump [m]
L_r = roller length in a dam-break wave [m]
Mo = Morton number, defined as Mo = We^3/(Fr^{2}Re^4) [–]
n = number of repetitions [–]
N = number of interfaces [–]

$\langle N \rangle$ = ensemble-median number of interfaces [–]
Re = Reynolds number, defined as $\mathrm{Re} = (\rho U h_0)/\mu$ [–]
t_{ch} = bubble chord time [s]
$t_{ch,med}$ = median bubble chord time [s]
T = time [s]
U = wavefront celerity [ms^{-1}]
V_1 = inflow velocity [ms^{-1}]
V_{max} = maximum value of the raw signal from a single probe-tip [V]
V_{min} = minimum value of the raw signal from a single probe-tip [V]
V_T = threshold value in air–water signal processing
We = Weber number, defined as $\mathrm{We} = (\rho h_0 U^2)/\sigma$ [–]
x = longitudinal distance [m]
y = cross-sectional distance [m]
z = vertical distance [m]
z_{90} = elevation where $C = 0.9$ [m]
z_{50} = elevation where $C = 0.5$ [m]
z_{10} = elevation where $C = 0.1$ [m]
$z_{c,max}$ = elevation where $C = C_{max}$ [m]
z^* = elevation of the transition between shear layer and recirculation zone [m]
ρ = water density, herein $\rho = 1000$ [kg m^{-3}]
μ = dynamic viscosity, herein $\mu = 1.002 \cdot 10^{-3}$ [Pa·s]
σ = surface tension, herein $\sigma = 0.07$ [kg s^{-2}]

CRediT authorship contribution statement

D. Regout: Writing – original draft, Visualization, Software, Resources, Project administration, Methodology, Investigation, Formal analysis, Data curation, Conceptualization. **S.N. Jonkman:** Writing – review & editing, Supervision. **D. Wüthrich:** Writing – review & editing, Validation, Supervision, Resources, Project administration, Methodology, Funding acquisition, Conceptualization.

Declaration of competing interest

The authors declare the following financial interests/personal relationships which may be considered as potential competing interests: Dorette Regout and Davide Wüthrich report financial support was provided by Dutch Research Council NWO. If there are other authors, they declare that they have no known competing financial interests or personal relationships that could have appeared to influence the work reported in this paper.

Acknowledgments

This study was supported by the Dutch Research Council NWO, The Netherlands (grant OCENW.XS21.2.045). The authors would like to thank the technical staff of the Hydraulic Laboratory at TU Delft, the Netherlands, for their technical support. Additionally, they acknowledge the assistance and contributions of Mr. Jonas Matsch, formerly an MSc student at TU Dresden, Germany, to the experimental work.

Data availability

Data will be made available on request.

References

Al-Faesly, T., Palermo, D., Nistor, I., Cornett, A., 2012. Experimental modeling of extreme hydrodynamic forces on structural models. Int. J. Prot. Struct. 3 (4), 477–506. http://dx.doi.org/10.1260/2041-4196.3.4.477.

Arnason, H., 2005. Interactions between an Incident Bore and a Free-Standing Coastal Structure (Ph.D. thesis). University of Washington.

Bai, Z., Bai, R., Tang, R., Wang, H., Liu, S., 2021. Case study of prototype hydraulic jump on slope: Air entrainment and free-surface measurement. J. Hydraul. Eng. 147 (9), http://dx.doi.org/10.1061/(asce)hy.1943-7900.0001916.

Bai, R., Zhang, F., Liu, S., Wang, W., 2016. Air concentration and bubble characteristics downstream of a chute aerator. Int. J. Multiph. Flow 87, 156–166. http://dx.doi.org/10.1016/j.ijmultiphaseflow.2016.07.007.

Brocchini, M., Peregrine, D.H., 2001. The dynamics of strong turbulence at free surfaces. Part 1. description. J. Fluid Mech. 449, 225–254. http://dx.doi.org/10.1017/S0022112001006012.

Bullock, G.N., Obhrai, C., Peregrine, D.H., Bredmose, H., 2007. Violent breaking wave impacts. Part 1: Results from large-scale regular wave tests on vertical and sloping walls. Coast. Eng. 54 (8), 602–617. http://dx.doi.org/10.1016/j.coastaleng.2006.12.002.

Çağatay, H., Kocaman, S., 2008. Experimental study of tailwater level effects on dam break flood wave propagation. In: River Flow 2008 : Proceedings of the International Conference on Fluvial Hydraulics. Cesme, Izmir, Turkey, pp. 635–644.

Cartellier, A., Achard, J.L., 1991. Local phase detection probes in fluid/fluid two-phase flows. Rev. Sci. Instrum. 62 (2), 279–303. http://dx.doi.org/10.1063/1.1142117.

Chachereau, Y., Chanson, H., 2011a. Bubbly flow measurements in hydraulic jumps with small inflow froude numbers. Int. J. Multiph. Flow 37 (6), 555–564. http://dx.doi.org/10.1016/j.ijmultiphaseflow.2011.03.012.

Chachereau, Y., Chanson, H., 2011b. Free-surface fluctuations and turbulence in hydraulic jumps. Exp. Therm Fluid Sci. 35 (6), 896–909. http://dx.doi.org/10.1016/j.expthermflusci.2011.01.009.

Chanson, H., 1989. Study of air entrainment and aeration devices. J. Hydraul. Res. 27 (3), 301–319. http://dx.doi.org/10.1080/00221688909499166.

Chanson, H., 1995. Air entrainment in two-dimensional turbulent shear flows with partially developed inflow conditions. Int. J. Multiph. Flow 21 (6), 1107–1121. http://dx.doi.org/10.1016/0301-9322(95)00048-3.

Chanson, H., 2004a. Hydraulics of Open Channel Flow: An Introduction, second ed. Butterworth-Heinemann, Oxford, United Kingdom.

Chanson, H., 2004b. Unsteady air-water flow measurements in sudden open channel flows. Exp. Fluids 37 (6), 899–909. http://dx.doi.org/10.1007/s00348-004-0882-3.

Chanson, H., 2007. Bubbly flow structure in hydraulic jump. Eur. J. Mech. B Fluids 26 (3), 367–384. http://dx.doi.org/10.1016/j.euromechflu.2006.08.001.

Chanson, H., 2009. Application of the method of characteristics to the dam break wave problem. J. Hydraul. Res. 47 (1), 41–49. http://dx.doi.org/10.3826/jhr.2009.2865.

Chanson, H., 2011. Hydraulic jumps: Turbulence and air bubble entrainment. Houille Blanche 3, 5–16. http://dx.doi.org/10.1051/lhb/2011026.

Chanson, H., 2020. Statistical analysis methods for transient flows–the dam-break case. J. Hydraul. Res. 58 (6), 1001–1004. http://dx.doi.org/10.1080/00221686.2020.1729266.

Chesters, A.K., 1975. The applicability of dynamic-similarity criteria to isothermal, liquid-gas, two-phase flows without mass transfer. Int. J. Multiph. Flow 2, 191–212.

Dressler, R.F., 1952. Hydraulic resistance effect upon the dam-break functions. Res. Natl. Bureau Stand. 49 (3).

Estrella, J., Wüthrich, D., Chanson, H., 2022a. Flow patterns, roller characteristics, and air entrainment in weak hydraulic jumps: Does size matter? J. Fluids Eng. Trans. ASME 144 (7), http://dx.doi.org/10.1115/1.4053581.

Estrella, J., Wüthrich, D., Chanson, H., 2022b. Two-phase air-water flows in hydraulic jumps at low froude number: Similarity, scale effects and the need for field observations. Exp. Therm Fluid Sci. 130, http://dx.doi.org/10.1016/j.expthermflusci.2021.110486.

Fuchs, H., 2013. Solitary Impulse Wave Run-Up and Overland Flow (Ph.D. thesis). ETH Zürich, Switzerland.

Hohermuth, B., Boes, R., Felder, S., 2021. High-velocity air-water flow measurements in a prototype tunnel chute: Scaling of void fraction and interfacial velocity. J. Hydraul. Eng. 147 (11), http://dx.doi.org/10.3929/ethz-b-000505832.

Kramer, M., Valero, D., 2020. Turbulence and self-similarity in highly aerated shear flows: The stable hydraulic jump. Int. J. Multiph. Flow 129, http://dx.doi.org/10.1016/j.ijmultiphaseflow.2020.103316.

Lauber, G., Hager, W.H., 1998. Experiments to dambreak wave: Horizontal channel. J. Hydraul. Res. 36 (3), 291–307. http://dx.doi.org/10.1080/00221689809498620.

Leng, X., Chanson, H., 2019. Air-water interaction and characteristics in breaking bores. Int. J. Multiph. Flow 120, http://dx.doi.org/10.1016/j.ijmultiphaseflow.2019.103101.

Lubin, P., Chanson, H., 2017. Are breaking waves, bores, surges and jumps the same flow? Environ. Fluid Mech. 17 (1), 47–77. http://dx.doi.org/10.1007/s10652-016-9475-y.

Lubin, P., Kimmoun, O., Véron, F., Glockner, S., 2019. Discussion on instabilities in breaking waves: Vortices, air-entrainment and droplet generation. Eur. J. Mech. B Fluids 73, 144–156. http://dx.doi.org/10.1016/j.euromechflu.2018.05.006.

Ma, J., Oberai, A.A., Lahey, R.T., Drew, D.A., 2011. Modeling air entrainment and transport in a hydraulic jump using two-fluid RANS and DES turbulence models. Heat Mass Transf. 47 (8), 911–919. http://dx.doi.org/10.1007/s00231-011-0867-8.

Madsen, P.A., Fuhrman, D.R., Schäffer, H.A., 2008. On the solitary wave paradigm for tsunamis. J. Geophys. Res.: Oceans 113 (12), http://dx.doi.org/10.1029/2008JC004932.

Montano, L., Felder, S., 2018. Effect of inflow conditions on the air-water flow properties in hydraulic jumps. In: Proceedings of the 21st Australasian Fluid Mechanics Conference. Adelaide, Australia, http://dx.doi.org/10.26190/unsworks/27044.

Montano, L., Felder, S., 2020. An experimental study of air–water flows in hydraulic jumps on flat slopes. J. Hydraul. Res. 58 (5), 767–777. http://dx.doi.org/10.1080/00221686.2019.1671512.

Mortazavi, M., Le Chenadec, V., Moin, P., Mani, A., 2016. Direct numerical simulation of a turbulent hydraulic jump: Turbulence statistics and air entrainment. J. Fluid Mech. 797, 60–94. http://dx.doi.org/10.1017/jfm.2016.230.

Murzyn, F., Mouaze, D., Chaplin, J.R., 2005. Optical fibre probe measurements of bubbly flow in hydraulic jumps. Int. J. Multiph. Flow 31 (1), 141–154. http://dx.doi.org/10.1016/j.ijmultiphaseflow.2004.09.004.

Nielsen, P., Xu, B., Wüthrich, D., Zhang, S., 2022. Friction effects on quasi-steady dam-break wave propagation on horizontal beds. J. Fluid Mech. 939, http://dx.doi.org/10.1017/jfm.2022.182.

Nouri, Y., Nistor, I., Palermo, D., Cornett, A., 2010. Experimental investigation of tsunami impact on free standing structures. Coast. Eng. J. 52 (1), 43–70. http://dx.doi.org/10.1142/S0578563410002117.

Ozmen-Cagatay, H., Kocaman, S., 2010. Dam-break flows during initial stage using SWE and RANS approaches. J. Hydraul. Res. 48 (5), 603–611. http://dx.doi.org/10.1080/00221686.2010.507342.

Pfister, M., Chanson, H., 2014. Two-phase air-water flows: Scale effects in physical modeling. J. Hydrodyn. 26 (2), 291–298. http://dx.doi.org/10.1016/S1001-6058(14)60032-9.

Pfister, M., Hager, W.H., 2014. History and significance of the morton number in hydraulic engineering. J. Hydraul. Eng. 140 (5), http://dx.doi.org/10.1061/(asce)hy.1943-7900.0000870.

Ritter, A., 1892. Die fortpflanzung der wasserwellen. Zeitschrift Verein Deutscher Ingenieure 36, 947–954.

Ryu, Y., Chang, K.A., Mercier, R., 2007. Application of dam-break flow to green water prediction. Appl. Ocean Res. 29 (3), 128–136. http://dx.doi.org/10.1016/j.apor.2007.10.002.

Shi, R., Wüthrich, D., Chanson, H., 2021. Air-water characteristics of a breaking bore roller, Part 2 : Air-water flow properties. Technical Report, School of Civil Engineering, The University of Queensland, Brisbane, Australia, ISBN: 9781742723396.

Shi, R., Wüthrich, D., Chanson, H., 2023a. Air–water properties of unsteady breaking bore part 2: Void fraction and bubble statistics. Int. J. Multiph. Flow 159, http://dx.doi.org/10.1016/j.ijmultiphaseflow.2022.104337.

Shi, R., Wüthrich, D., Chanson, H., 2023b. Air–water properties of unsteady breaking bores part 1: Novel Eulerian and Lagrangian velocity measurements using intrusive and non-intrusive techniques. Int. J. Multiph. Flow 159, http://dx.doi.org/10.1016/j.ijmultiphaseflow.2022.104338.

Shi, R., Wüthrich, D., Chanson, H., 2023c. Discussion of "performance of intrusive phase-detection probe with large sensor size in air-water flow measurement and application to prototype hydraulic jump study". J. Hydraul. Eng. 149 (11), http://dx.doi.org/10.1061/jhend8.hyeng-13563.

Stansby, P.K., Chegini, A., Barnes, T.C., 1998. The initial stages of dam-break flow. J. Fluid Mech. 370, 203–220. http://dx.doi.org/10.1017/S0022112098001918.

Stoker, J., 1957. Water waves. Interscience.

Wang, H., 2014. Turbulence and Air Entrainment in Hydraulic Jumps (Ph.D. thesis). The University of Queensland, Brisbane, Australia.

Wang, H., Murzyn, F., 2017. Experimental assessment of characteristic turbulent scales in two-phase flow of hydraulic jump: from bottom to free surface. Environ. Fluid Mech. 17 (1), 7–25. http://dx.doi.org/10.1007/s10652-016-9451-6.

Whitham, G.B., 1955. The effects of hydraulic resistance in the dam-break problem. In: Proceedings of the Royal Society of London. Series a, Mathematical and Physical Sciences, Vol. 227, No. 1170. pp. 399–407.

Witt, A., Gulliver, J., Shen, L., 2015. Simulating air entrainment and vortex dynamics in a hydraulic jump. Int. J. Multiph. Flow 72, 165–180. http://dx.doi.org/10.1016/j.ijmultiphaseflow.2015.02.012.

Wüthrich, D., Pfister, M., Nistor, I., Schleiss, A.J., 2018. Experimental study of tsunami-like waves generated with a vertical release technique on dry and wet beds. J. Waterway, Port, Coastal Ocean Engrg. 114 (4), http://dx.doi.org/10.1061/(ASCE)WW.1943-5460.0000447.

Wüthrich, D., Regout, D., 2024. Air-water flow properties in dam-break waves: a sensitivity analysis. In: Proceedings of the 10th International Symposium on Hydraulic Structures. Zurich, Switzerland, pp. 166–175. http://dx.doi.org/10.3929/ethz-b-000675959.

Wüthrich, D., Shi, R., Chanson, H., 2021. Strong free-surface turbulence in breaking bores: A physical study on the free-surface dynamics and air-water interfacial features. J. Fluid Mech. 924, http://dx.doi.org/10.1017/jfm.2021.614.

Wüthrich, D., Shi, R., Chanson, H., 2022a. Ensemble-statistical approach in the measurement of air-water flow properties in highly unsteady breaking bores. Rev. Sci. Instrum. 93 (5), http://dx.doi.org/10.1063/5.0077774.

Wüthrich, D., Shi, R., Chanson, H., 2022b. Hydraulic jumps with low inflow froude numbers: air–water surface patterns and transverse distributions of two-phase flow properties. Environ. Fluid Mech. 22 (4), 789–818. http://dx.doi.org/10.1007/s10652-022-09854-5.

Yang, S., Yang, W., Qin, S., Li, Q., Yang, B., 2018. Numerical study on characteristics of dam-break wave. Ocean Eng. 159, 358–371. http://dx.doi.org/10.1016/j.oceaneng.2018.04.011.

Yang, S., Yang, W., Zhang, C., Qin, S., Wei, K., Zhang, J., 2022. Experimental and numerical study on the evolution of wave front profile of dam-break waves. Ocean Eng. 247, http://dx.doi.org/10.1016/j.oceaneng.2022.110681.

Ye, Y., Xu, T., Zhu, D.Z., 2020. Numerical analysis of dam-break waves propagating over dry and wet beds by the mesh-free method. Ocean Eng. 217, http://dx.doi.org/10.1016/j.oceaneng.2020.107969.

Zabaleta, F., Márquez Damián, S., Bombardelli, F.A., 2023. A novel three-phase mixture approach for the numerical modeling of self-aerated flows. Comput. Methods Appl. Mech. Engrg. 408, http://dx.doi.org/10.1016/j.cma.2023.115958.

Zhou, X., Su, L., He, X., Hu, R., Yuan, H., 2024. Experimental investigations of propagation characteristics and wave energy of dam-break waves on wet bed. Ocean Eng. 301, http://dx.doi.org/10.1016/j.oceaneng.2024.117566.

Zuo, J., Xu, T., Zhu, D.Z., Gu, H., 2022. Impact pressure of dam-break waves on a vertical wall with various downstream conditions by an explicit mesh-free method. Ocean Eng. 256, http://dx.doi.org/10.1016/j.oceaneng.2022.111569.